

Molecular magnetic hysteresis at 60 K in dysprosocenium

DOI:

[10.1038/nature23447](https://doi.org/10.1038/nature23447)

Document Version

Accepted author manuscript

[Link to publication record in Manchester Research Explorer](#)

Citation for published version (APA):

Goodwin, C., Ortu, F., Reta, D., Chilton, N., & Mills, D. (2017). Molecular magnetic hysteresis at 60 K in dysprosocenium. *Nature*, 548, 439-442. <https://doi.org/10.1038/nature23447>

Published in:

Nature

Citing this paper

Please note that where the full-text provided on Manchester Research Explorer is the Author Accepted Manuscript or Proof version this may differ from the final Published version. If citing, it is advised that you check and use the publisher's definitive version.

General rights

Copyright and moral rights for the publications made accessible in the Research Explorer are retained by the authors and/or other copyright owners and it is a condition of accessing publications that users recognise and abide by the legal requirements associated with these rights.

Takedown policy

If you believe that this document breaches copyright please refer to the University of Manchester's Takedown Procedures [<http://man.ac.uk/04Y6Bo>] or contact uml.scholarlycommunications@manchester.ac.uk providing relevant details, so we can investigate your claim.



Molecular magnetic hysteresis at 60 K in dysprosocenium

Conrad A. P. Goodwin¹, Fabrizio Ortu¹, Daniel Reta¹, Nicholas F. Chilton¹ & David P. Mills¹

¹School of Chemistry, The University of Manchester, Oxford Road, Manchester, M13 9PL, UK.

Lanthanides have been extensively investigated for potential applications in quantum information processing and high-density data storage at the molecular and atomic scale; remarkable experimental achievements include reading and manipulating single nuclear spins^{1,2}, exploiting atomic clock transitions for robust qubits³, and most recently magnetic data storage in single atoms^{4,5}. Single molecule magnets (SMMs) display magnetic hysteresis of molecular origin⁶ – a magnetic memory effect and a prerequisite of data storage – and lanthanide examples have exhibited this phenomenon at the highest temperatures to date. However, in nearly 25 years since the landmark discovery of SMMs⁷ hysteresis temperatures have only increased from 4 K to ~14 K⁸⁻¹⁰ (using a consistent magnetic field sweep rate of *ca.* 20 Oe s⁻¹, though higher temperatures have been achieved by using very fast sweep rates,^{11,12} e.g. 30 K with 200 Oe s⁻¹)¹². Here we report a hexa-*tert*-butyldysprosocenium complex, [Dy(Cp^{ttt})₂][B(C₆F₅)₄] [1; Cp^{ttt} = {C₅H₂^tBu_{3-1,2,4}}; ^tBu = C(CH₃)₃], which shows magnetic hysteresis up to 60 K at 22 Oe s⁻¹. We observe a clear change in the relaxation dynamics at this temperature, which persists in magnetically diluted samples, suggesting that the origin of the hysteresis is the localised metal-ligand vibrational modes unique to dysprosocenium. *Ab initio* spin dynamics demonstrate that magnetic relaxation at high temperatures is due to local molecular vibrations, and thus indicate that with judicious molecular design, magnetic data storage in single molecules at temperatures above liquid nitrogen may become possible.

Metalloccenium cations are positively charged species that contain a metal ion sandwiched between two aromatic π -ligands; the *bis*-cyclopentadienyl (Cp) family is the classical example. The isolation of $[\text{Ln}(\text{Cp}^{\text{R}})_2]^+$ (Ln = lanthanide; $\text{Cp}^{\text{R}} = \text{C}_5\text{R}_5$; R = H, alkyl or silyl) has proved problematic because lanthanide bonding is predominantly ionic and Ln(III) cations are relatively large, thus additional ligands tend to coordinate equatorially. Notably, the nearest structurally characterised lanthanide and rare earth examples reported to date, $[\text{Sm}\{\text{C}_5\text{Me}_4(\text{SiMe}_2\text{CH}_2\text{CH}=\text{CH}_2)\}_2][\text{BPh}_4]$ (Me = CH₃, Ph = C₆H₅)¹³, $[\text{Sc}(\text{Cp}^*)_2\{\mu-(\text{C}_6\text{F}_5)_2\text{B}(\text{C}_6\text{F}_5)_2\}](\text{Cp}^* = \text{C}_5\text{Me}_5)$ ¹⁴, $[\{\text{Ln}(\text{Cp}^*)_2\}_2\{\mu-(\text{C}_6\text{F}_5)_2\text{B}(\text{C}_6\text{F}_5)_2\}_2]$ (Ln = Pr, Nd)¹⁵ and $[\text{Dy}(\text{Cp}^*)_2\{\mu-(\text{Ph})_2\text{BPh}_2\}]$ ^{16,17} all feature weak equatorial ligand interactions. Recently, the elusive dysprosocenium cation had become a significant synthetic target¹⁸ because the near-cylindrical symmetry and axial concentration of negative charge should give a very high energy barrier to magnetic relaxation^{19,20} and hence possibly allow magnetic hysteresis at relatively high temperatures. However, some ligand fields are better suited to Ln(III) cations where the most magnetic states are prolate in nature; e.g. $[\text{Er}(\text{C}_8\text{H}_8)(\text{Cp}^*)]$ exhibits hysteresis up to 5 K²¹ but for $[\text{Dy}(\text{C}_8\text{H}_8)(\text{Cp}^*)]$ ²² and $[\text{Dy}\{\text{C}_8\text{H}_6(\text{SiMe}_3)_{2-1,4}\}_2\text{Li}(\text{THF})(\text{DME})]$ ²³ this behaviour is not observed above 1.8 K (all ca. 20 Oe s⁻¹), and $[\text{Er}\{\text{N}(\text{SiMe}_3)_2\}_3]$ shows hysteresis while $[\text{Dy}\{\text{N}(\text{SiMe}_3)_2\}_3]$ does not²⁴.

Complex **1** was synthesised by the reaction of $[\text{Dy}(\text{Cp}^{\text{ttt}})_2(\text{Cl})]$ with the silylium reagent $[\text{H}(\text{SiEt}_3)_2][\text{B}(\text{C}_6\text{F}_5)_4]$ (Et = CH₂CH₃) in benzene at room temperature (Fig. 1)²⁵. Guo *et al.* have simultaneously reported the synthesis and magnetic data for **1**²⁶. Bright yellow crystals of **1** were obtained in 60% yield by layering a saturated DCM solution of crude material with hexane at 4 °C, followed by storage at -25 °C. Detailed synthetic information and full characterisation of all compounds is given in the Supplementary Information. Crucially, single crystal X-ray diffraction studies show no appreciable interactions of the $\{\text{B}(\text{C}_6\text{F}_5)_4\}$ anion with the cation in **1** [shortest equatorial Dy...F distance: 5.996(3) Å], due to the steric demands of the six ^tBu groups, though

two short intramolecular Dy \cdots C_{methyl} distances [2.964(5) Å mean] produce an approximately linear H \cdots Dy \cdots H motif [174.96°; Dy \cdots H: 2.4989 Å mean]. The bent dysprosocenium cation exhibits a Cp_{centroid1} \cdots Dy \cdots Cp_{centroid2} angle of 152.56(7)° with the two C₅ rings approximately eclipsed, in contrast with [Dy(Cp*)₂{μ-(Ph)₂BPh₂}] [Cp_{centroid1} \cdots Dy \cdots Cp_{centroid2} = 134.00(4)°], which adopts a staggered conformation¹⁶. The mean Dy \cdots Cp_{centroid} distance in **1** is relatively short [2.316(3) Å], as expected from electrostatic considerations for an isolated cation *cf.* [Dy(Cp*)₂{μ-(Ph)₂BPh₂}] [2.373(2) Å]¹⁶. Complete active space self-consistent field spin-orbit (CASSCF-SO) calculations on the X-ray structure of **1** show that it possesses large easy-axis magnetic anisotropy (Fig. 4b, Table S13), and thus should exhibit SMM behaviour. Further calculations show that the close equatorial H atoms, the bent geometry, and the eclipsed rings do not make significant contributions to the electronic structure of **1** (Tables S14 – S16).

Magnetic measurements reveal that **1** shows open hysteresis at and below 60 K using a sweep rate of 22 Oe s⁻¹, with 83% remanent magnetisation and a coercive field of 20 – 25 kOe at 2 K (Fig. 2). The low temperature hysteresis data show a step at zero-field, likely due to enhanced relaxation by quantum tunnelling of the magnetisation (QTM), a common feature in SMMs⁶. To confirm that the magnetic hysteresis is of molecular origin and does not owe to long-range ordering, we have measured a structurally analogous doped sample, 8% Dy@[Y(Cp^{ttt})₂][B(C₆F₅)₄] **2**, and two frozen dichloromethane solutions of **1** with concentrations *ca.* 21 mM, **3**, and 170 mM, **4**, (Figs. S32 – S35, Table S3); these samples also show hysteretic behaviour, confirming these properties are intrinsic to the [Dy(Cp^{ttt})₂]⁺ cation. Interestingly, while the zero-field step is reduced for **2** (Figs. S32 and S35), suggesting that dipolar interactions are partially responsible for this feature in **1**, the step is more significant for the DCM solution samples **3** and **4** (Figs. S33 – S35), implying that the local environment of the molecule plays a crucial role in the zero-field dynamics. Similar results are found for a solution sample with an alternative solvent, 1,2-difluorobenzene (Fig. S35), indicating that this step is not due to

coordination of DCM. Despite the faster zero-field relaxation, hysteresis still persists up to at least 54 K for **4** (Fig. S34). Field cooled (FC) and zero-field cooled (ZFC) magnetic susceptibility, χ , for **1-4** coincide with the theoretical equilibrium trace until 61 K, below which they bifurcate and are out of equilibrium (Figs. 3a and S36 – S39).

To probe the origin of the magnetic hysteresis, we measured the magnetic relaxation rate by alternating current (AC) magnetic susceptibility and direct current (DC) magnetisation decay. The out-of-phase component of the AC susceptibility, χ'' , of **1** exhibits frequency dependent peaks between 72 and 112 K (Fig. S40), and fitting these data with the Debye model⁶ shows that the relaxation rate follows an Arrhenius law $\tau^{-1} = \tau_0^{-1} \exp[-U_{\text{eff}}/kT]$ with $U_{\text{eff}} = 1223 \text{ cm}^{-1}$ (1760 K) and $\tau_0 = 1.986 \times 10^{-11} \text{ s}$ (Figs. 3b and S56); this is consistent with an Orbach relaxation mechanism over an effective energy barrier, U_{eff} . To extend investigation of the relaxation dynamics to lower temperatures, we measured the DC magnetisation decay between 26 and 62 K; fitting these data with single exponentials⁶ yields the magnetic relaxation rates (Figs. S43 – S46, Table S8). Between 26 and 50 K the relaxation rate has a power-law dependence on temperature and is well-modelled by $\tau^{-1} = CT^n$ with $C = 1.664 \times 10^{-6} \text{ s}^{-1} \text{ K}^{-n}$ and $n = 2.151$ (Figs. 3b and S57). While the value of n is close to that expected for a phonon bottleneck ($n = 2$)²⁷, the relaxation rates for the doped and solution samples **2-4** follow almost exactly the same temperature dependence as **1** (Figs. S58 – S61), and thus these dynamics are intrinsic to the $[\text{Dy}(\text{Cp}^{\text{ttt}})_2]^+$ cation and not the result of inefficient heat flow between the lattice and the bath. Intriguingly, the intersection of the exponential and power-law dynamics occurs at 60.4 K for **1**, coincident with the temperature at which magnetic hysteresis appears and the FC/ZFC susceptibilities bifurcate.

The computational and magnetic data for **1** are generally in excellent agreement with those reported by Guo *et al.*²⁶. Slight differences are observed in the FC/ZFC behaviour, likely due to different temperature sweep rates having a profound effect on the relaxation dynamics

below 61 K. The origin of the discrepancy between the power-law relaxation exponents ($n = 2.151$ vs. 3.92^{26}) is not obvious. However, we find consistent behaviour for samples of different concentrations and phases, and at lower temperatures (Fig. S61), thus we suggest that the results herein show the intrinsic properties of **1**.

To investigate the mechanism of magnetic relaxation, we have undertaken an *ab initio* study of the spin dynamics; such approaches have only recently become viable^{28,29}. Magnetic relaxation in SMMs is effected by the coupling of the electronic states to the quantised vibrational modes of the lattice (phonons). However, as the relaxation dynamics for $[\text{Dy}(\text{Cp}^{\text{ttt}})_2]^+$ are consistent between the crystalline phase and amorphous frozen solution, we hypothesise that magnetic relaxation is moderated by localised molecular vibrations (optical phonons). Thus, as a first approximation we consider only the gas-phase vibrational modes of the $[\text{Dy}(\text{Cp}^{\text{ttt}})_2]^+$ cation. Our approach consists of four stages: (i) calculation and (ii) calibration of vibrational modes; (iii) calculation of spin-phonon coupling; and, (iv) simulation of dynamics. We calculate the vibrational modes with density functional theory, and calibrate the vibrational energies and atomic displacements by comparison to the vibrational spectra (Fig. S63, Table S19) and to the thermal displacement parameters from X-ray diffraction, respectively. We determine the spin-phonon coupling by performing a CASSCF-SO calculation for each vibrational mode on molecular geometries distorted from equilibrium along the relevant normal mode vector, followed by a crystal field decomposition of the electronic structure; thus, we define the electronic part of the spin-phonon coupling from the change in the crystal field potential. We then calculate the transition rates between each electronic state by allowing a finite Gaussian linewidth, σ , for each vibrational mode and finally simulate the spin dynamics by solution to the master equation⁶.

Considering single-phonon transitions (Table S22), we find one slow relaxation rate (Table S23) corresponding to the Orbach mechanism; this result echoes the archetypal case of

Mn₁₂⁶. As a function of temperature, the calculated relaxation rate reproduces the slope of the AC data well (Figs. 4a and S65), demonstrating that the Orbach mechanism is moderated by local molecular vibrations. Variation of σ slightly affects the effective pre-factor τ_0^{-1} of the Orbach mechanism (Fig. S65), but we fix $\sigma = 10 \text{ cm}^{-1}$ to be consistent with the full-width-half-maximum linewidth of the experimental vibrational spectra. Given our approximations, the agreement between our *ab initio* spin-dynamics and experimental measurements is remarkable. The calculated transition rates reveal a heterogeneous relaxation pathway that does not proceed through all states sequentially; the most probable pathway for Orbach relaxation is $|\pm 15/2\rangle \rightarrow |\pm 13/2\rangle \rightarrow |\pm 11/2\rangle \rightarrow |\pm 9/2\rangle \rightarrow |\pm 5/2\rangle \rightarrow |\mp 3/2\rangle \rightarrow |\mp 7/2\rangle \rightarrow |\mp 11/2\rangle \rightarrow |\mp 13/2\rangle \rightarrow |\mp 15/2\rangle$ (Fig. 4b, Table S24). Decomposing the transition rates further, it is the vibrational motion of the C–H groups on the Cp^{ttt} rings that facilitate the initial $|\pm 15/2\rangle \rightarrow |\pm 13/2\rangle$ relaxation step (Fig. S66, Table S25). Therefore, we propose that substitution of these groups would significantly affect the relaxation dynamics and possibly lead to magnetic hysteresis at higher temperatures.

Considering the two-phonon second-order Raman process (Table S26), we find three slow relaxation rates (Table S27), however only one contributes to the relaxation dynamics. While we have shown that the low-temperature $\tau^{-1} \propto T^2$ region is not due to a phonon bottleneck, the temperature dependence of the calculated Raman mechanism deviates considerably from the experiment, a feature that is not improved by altering σ (Fig. 4a and S67). This could be due to our gas-phase approximation which lacks the true dispersion of the optical modes and their coupling to the acoustic modes³⁰, or to the neglect of explicit anharmonicity²⁸.

Whilst simple electrostatic models have predicted that the quintessential Ln SMM should be a Dy(III) complex with negatively charged ligands along a single axis^{19,20}, and considerable magnetic anisotropy has been achieved for such complexes^{9-12,31}, until now a thirty-fold increase in the largest U_{eff} barrier ($\sim 42 \text{ cm}^{-1}$ ⁷ to 1261 cm^{-1} ¹⁰) had been accompanied by only a four-fold

increase in the highest temperature at which magnetic hysteresis was observed (4 K^7 to 14 K^{8-10} at *ca.* 20 Oe s^{-1}). The U_{eff} value for **1** is similar to that of 1261 cm^{-1} for $[\text{Dy}(\text{tBuO})_2(\text{pyridine})_5][\text{BPh}_4]^{10}$, however the highest temperature at which magnetic hysteresis is observed is substantially larger (60 K vs. 3 K) and there is significantly more remanent magnetisation at 2 K (83% vs. *ca.* 11%). Furthermore, the zero-field step observed here is much smaller than for other Dy(III) SMMs^{9-12,31}, suggesting that such steps which plague SMMs are not solely due to hyperfine coupling or local dipolar fields as is routinely suggested. We theorise that the lack of a severe zero-field step and the notably improved relaxation dynamics for **1** are due to the unique spin-phonon coupling of the constrained metal-ligand vibrational modes intrinsic to the bis- $\eta^5\text{-Cp}^{\text{ttt}}$ coordination geometry. This is in contrast to other molecules with large U_{eff} that do not show hysteresis at comparably high temperatures, for example $[\text{Dy}(\text{tBuO})_2(\text{pyridine})_5][\text{BPh}_4]^{10}$, where the first coordination sphere is constructed from mono-atomic donors which have greater metal-ligand flexibility.

1. Vincent, R., Klyatskaya, S., Ruben, M., Wernsdorfer, W., Balestro, F. Electronic read-out of a single nuclear spin using a molecular spin transistor. *Nature* **488**, 357–360 (2012).
2. Thiele, S., Balestro, F., Ballou, R., Klyatskaya, S., Ruben, M., Wernsdorfer, W. Electrically driven nuclear spin resonance in single-molecule magnets. *Science* **344**, 1135–1138 (2014).
3. Shiddiq, M., Komijani, D., Duan, Y., Gaita-Ariño, A., Coronado, E., Hill, S. Enhancing coherence in molecular spin qubits *via* atomic clock transitions. *Nature* **531**, 348–351 (2016).
4. Donati, F., Rusponi, S., Stepanow, S., Wäckerlin, C., Singha, A., Persichetti, L., Baltic, R., Diller, K., Patthey, F., Fernandes, E., Dreiser, J., Šljivančanin, Ž., Kummer, K., Nistor, C., Gambaradella, P., Brune, H. Magnetic remanence in single atoms. *Science* **352**, 318–321 (2016).

5. Natterer, F. D. Yang, K., Paul, W., Willke, P., Choi, T., Greber, T., Heinrich, A. J., Lutz, C. P. Reading and writing single-atom magnets. *Nature* **543**, 226–228 (2017).
6. Gatteschi, D., Sessoli, R., Villain, J. Molecular Nanomagnets. Oxford University Press (2006).
7. Sessoli, R., Gatteschi, D., Caneschi, A., Novak, M. A. Magnetic bistability in a metal-ion cluster. *Nature* **365**, 141–143 (1993).
8. Rinehart, J. D., Fang, M., Evans, W. J., Long, J. R. A N_2^{3-} Radical-Bridged Terbium Complex Exhibiting Magnetic Hysteresis at 14 K. *J. Am. Chem. Soc.* **133**, 14236–14239 (2011).
9. Liu, J., Chen, Y.-C., Liu, J.-L., Vieru, V., Ungur, L., Jia, J.-H., Chibotaru, L. F., Lan, Y., Wernsdorfer, W., Gao, S., Chen, X.-M., Tong, M.-L. A stable pentagonal bipyramidal Dy(III) single-ion magnet with a record magnetization reversal barrier over 1000 K. *J. Am. Chem. Soc.* **138**, 5441–5450 (2016).
10. Ding, Y.-S., Chilton, N. F., Winpenny, R. E. P., Zheng, Y.-Z. On approaching the limit of molecular magnetic anisotropy: a near-perfect pentagonal bipyramidal dysprosium(III) single-molecule magnet. *Angew. Chem. Int. Ed.* **55**, 16071–16074 (2016).
11. Chen, Y.-C., Liu, J.-L., Ungur, L., Liu, J., Li, Q.-W., Wang, L.-F., Ni, Z.-P., Chibotaru, L. F., Chen, X.-M., Tong, M.-L. Symmetry-supported magnetic blocking at 20 K in pentagonal bipyramidal Dy(III) single-ion magnets. *J. Am. Chem. Soc.* **138**, 2829–2837 (2016).
12. Gupta, S. K., Rajeshkumar, T., Rajaraman, G., Murugavel, R. An air-stable Dy(III) single-ion magnet with high anisotropy barrier and blocking temperature. *Chem. Sci.* **7**, 5181–5191 (2016).
13. Evans, W. J., Perotti, J. M., Brady, J. C., Ziller, J. W. Tethered olefin studies of alkene versus tetraphenylborate coordination and lanthanide olefin interactions in metallocenes. *J. Am. Chem. Soc.* **125**, 5204–5212 (2003).

14. Berkefeld, A., Piers, W. E., Parvez, M., Castro, L., Maron, L., Eisenstein, O. Carbon monoxide activation via O=bound CO using decamethylscandocinium-hydridoborate ion pairs. *J. Am. Chem. Soc.* **134**, 10843–10851 (2014).
15. Kaita, S., Hou, Z., Nishiura, M., Doi, Y., Kurazumi, J., Horiuchi, A. C., Wakatsuki, Y. Ultimately specific 1,4-cis polymerization of 1,3-butadiene with a novel gadolinium catalyst. *Macromol. Rapid Commun.* **24**, 179–184 (2003).
16. Demir, S., Zadrozny, J. M., Nippe, M., Long, J. R. Exchange coupling and magnetic blocking in bipyrimidyl radical-bridged dilanthanide complexes. *J. Am. Chem. Soc.* **134**, 18546–18549 (2012).
17. Demir, S., Zadrozny, J. M., Long, J. R. Large spin-relaxation barriers for the low-symmetry organolanthanide complexes $[\text{Cp}^*_2\text{Ln}(\text{BPh}_4)]$ (Cp^* =pentamethylcyclopentadienyl; $\text{Ln}=\text{Tb}, \text{Dy}$). *Chem. Eur. J.* **20**, 9524–9529 (2014).
18. Meng, Y.-S., Zhang, Y.-Q., Wang, Z.-M., Wang, B.-W., Gao, S. Weak ligand-field effect from ancillary ligands on enhancing single-ion magnet performance. *Chem. Eur. J.* **22**, 12724–12731 (2016).
19. Rinehart, J. D., Long, J. R. Exploiting single-ion anisotropy in the design of f-element single-molecule magnets. *Chem. Sci.* **2**, 2078–2085 (2011).
20. Chilton, N. F., Collison, D., McInnes, E. J. L., Winpenny, R. E. P., Soncini, A. An electrostatic model for the determination of magnetic anisotropy in dysprosium complexes. *Nature Commun.* **4**, 2551 (2013).
21. Jiang, S.-D., Wang, B.-W., Sun, H.-L., Wang, Z.-M., Gao, S. An organometallic single-ion magnet. *J. Am. Chem. Soc.* **133**, 4730–4733 (2011).
22. Jiang, S.-D., Liu, S.-S., Zhou, L.-N., Wang, B.-W., Wang, Z.-M., Gao, S. Series of lanthanide organometallic single-ion magnets. *Inorg. Chem.* **51**, 3079–3087 (2012).

23. Jeletic, M., Lin, P.-H., Le Roy, J. J., Korobkov, I., Gorelsky, S. I., Murugesu, M. An organometallic sandwich lanthanide single-ion magnet with an unusual multiple relaxation mechanism. *J. Am. Chem. Soc.* **133**, 19286–19289 (2011).
24. Zhang, P., Zhang, L., Wang, C., Xue, S., Lin, S.-Y., Tang, J. Equatorially coordinated lanthanide single ion magnets. *J. Am. Chem. Soc.* **136**, 4484–4487 (2014).
25. Stoyanov, E. S., Stoyanova, I. V., Reed, C. A. The basicity of unsaturated hydrocarbons as probed by hydrogen-bond-acceptor ability: bifurcated N–H⁺--- π hydrogen bonding. *Chem. Eur. J.* **14**, 7880–7891 (2008).
26. Guo, F.-S., Day, B. J., Chen, Y.-C., Tong, M.-L., Mansikkamäki, A., Layfield, R. A. A dysprosium metallocenium single-molecule magnet functioning at the axial limit. *Angew. Chem. Int. Ed.* DOI:10.1002/anie.201705426.
27. Abragam, A., Bleaney, B. Electron Paramagnetic Resonance of Transition Ions. Oxford University Press (1970).
28. Lunghi, A., Totti, F., Sessoli, R., Sanvito, S. The role of anharmonic phonons in under-barrier spin relaxation of single molecule magnets. *Nature Commun.* **8**, 14620 (2017).
29. Escalera-Moreno, L., Suaud, N., Gaita-Ariño, A., Coronado, E. Determining key local vibrations in the relaxation of molecular spin qubits and single-molecule magnets. *J. Phys. Chem. Lett.* **8**, 1695–1700 (2017).
30. Shrivastava, K. N. Theory of Spin–Lattice Relaxation. *Phys. Stat. Sol. (B)* **117**, 437–458 (1983).
31. Gregson, M., Chilton, N. F., Ariciu, A.-M., Tuna, F., Crowe, I. F., Lewis, W., Blake, A. J., Collison, D., McInnes, E. J. L., Winpenny, R. E. P., Liddle, S. T. A monometallic lanthanide bis(methanediide) single molecule magnet with a large energy barrier and complex spin relaxation behaviour. *Chem. Sci.* **7**, 155–165 (2016).

Supplementary Information is linked to the online version of the paper at
www.nature.com/nature.

Acknowledgments We acknowledge funding from the Engineering and Physical Sciences
Research Council (studentship to C.A.P.G. and EP/P002560/1 for F.O. and D.R.), the Ramsay
Memorial Fellowships Trust (fellowship to N.F.C.) and The University of Manchester. We thank
the EPSRC U.K. National Electron Paramagnetic Resonance Service for access to the SQUID
magnetometer and Profs. R. E. P. Winpenny, E. J. L. McInnes and D. Collison for comments.

Author contributions C.A.P.G. and D.P.M. provided the original concept. C.A.P.G.
synthesised and characterised the compounds. F.O. carried out the single crystal X-ray
diffraction analysis and supporting synthetic/characterisation work. N.F.C. collected and
interpreted magnetic data. N.F.C. devised the relaxation dynamics model and wrote computer
programs to perform these calculations. D.R. and N.F.C. performed the calculations. D.P.M. and
N.F.C. wrote the manuscript with contributions from all authors. D.P.M. and N.F.C. supervised
the project.

Author Information Reprints and permissions information is available at
www.nature.com/reprints. The authors declare no competing financial interests.
Correspondence and requests for materials should be addressed to D.P.M.
(david.mills@manchester.ac.uk) and N.F.C. (nicholas.chilton@manchester.ac.uk).

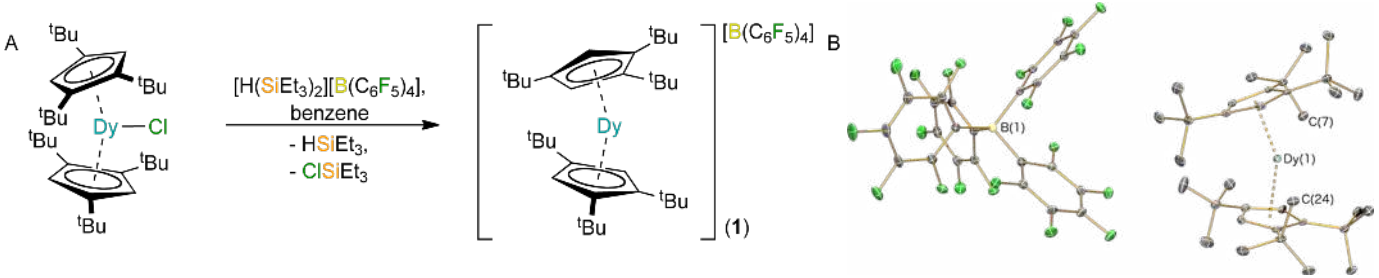
Data availability CCDC 1542354–1542357 contain the supplementary crystal data for this article. These data can be obtained free of charge from the Cambridge Crystallographic Data Centre via www.ccdc.cam.ac.uk/data_request/cif. Research data files supporting this publication are available from Mendeley Data at doi:10.17632/sj5t9dy53s.1. All other datasets generated and analysed during the current study are available from the corresponding authors on reasonable request.

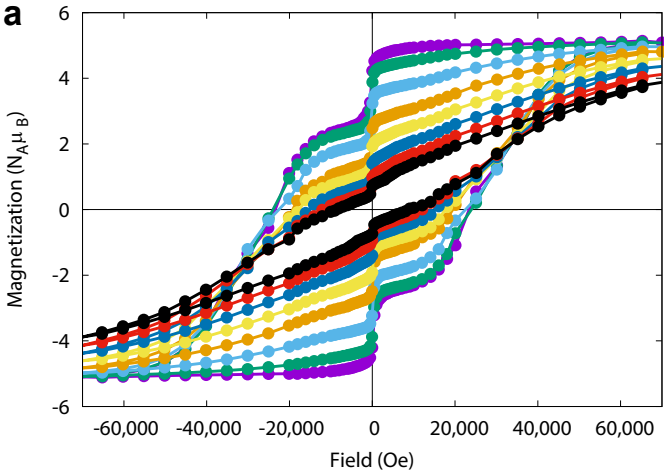
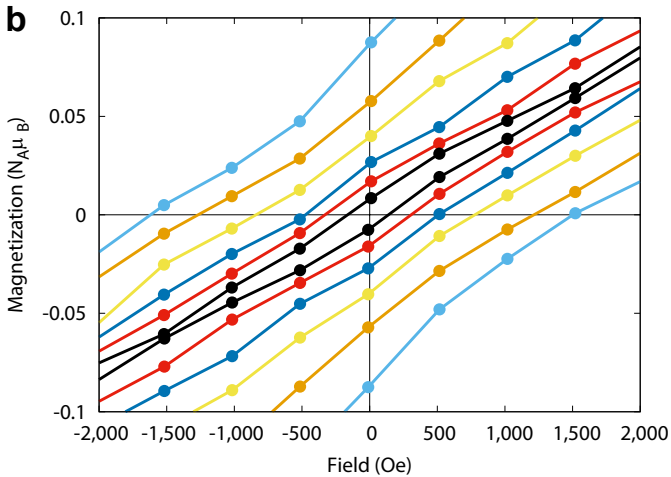
Figure 1 | Synthesis and structure of $[\text{Dy}(\text{Cp}^{\text{ttt}})_2][\text{B}(\text{C}_6\text{F}_5)_4]$ (1). **a**, Synthesis of **1**. **b**, Molecular structure of **1** with selective atom labelling (B = yellow, C = grey, Dy = cyan, F = green). Displacement ellipsoids set at 30 % probability level and hydrogen atoms are omitted for clarity. Selected distances and angles: Dy1...Cp_{centroid1}, 2.318(2) Å; Dy1...Cp_{centroid2}, 2.314(2) Å; Dy1...C7, 2.971(5) Å; Dy1...C24, 2.956(5) Å; Cp_{centroid1}...Dy1...Cp_{centroid2}, 152.56(7)°.

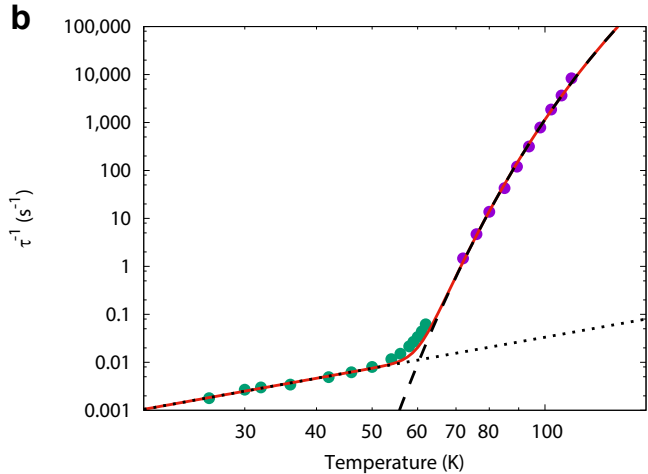
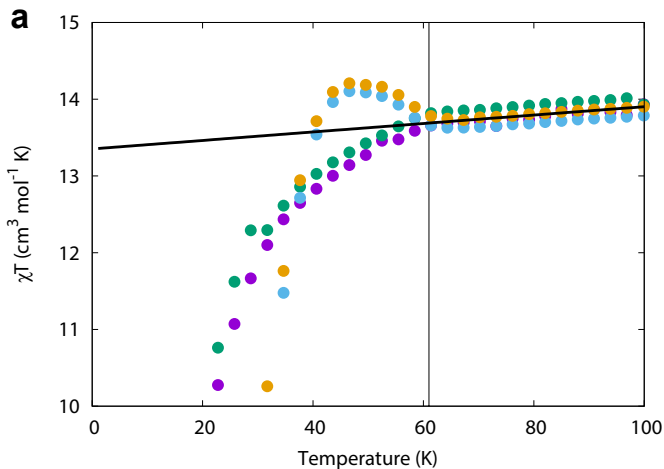
Figure 2 | Magnetic hysteresis of 1. Hysteresis was measured with a mean field sweep rate of 22(9) Oe s⁻¹ for |H| < 10 kOe, 54(15) Oe s⁻¹ for 10 < |H| < 20 kOe, and 91(17) Oe s⁻¹ for 20 < |H| < 70 kOe, giving an overall mean sweep rate of 50(33) Oe s⁻¹. The sweep rate was slow (22 Oe s⁻¹) around zero-field where the relaxation dynamics of SMMs are crucially dependent on sweep rate. **a**, Hysteresis loops recorded at 2 (purple) – 30 K (black) in 4 K steps. **b**, Hysteresis loops recorded at 52 (blue) – 60 (red) and 62 K (black) in 2 K steps, with truncated x- and y-axes, showing open hysteresis at 60 K but closed at 62 K.

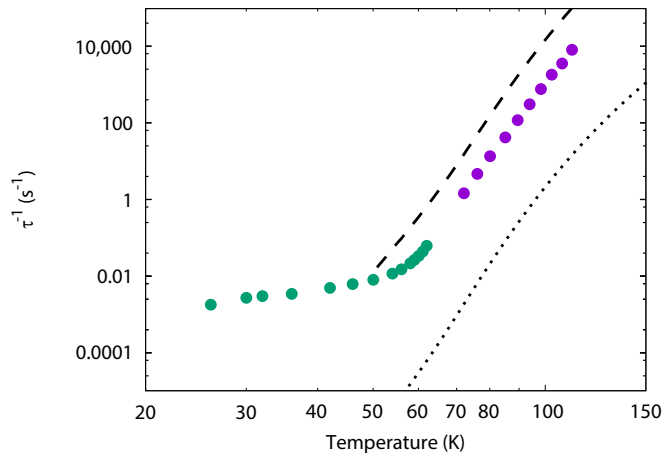
Figure 3 | Relaxation dynamics of 1. **a**, FC and ZFC magnetic susceptibilities (as χT product) at 1 kOe FC (purple), 500 Oe FC (green), 1 kOe ZFC (light blue) and 500 Oe ZFC (orange), with the CASSCF-SO-calculated curve scaled by 1.08 (black line). Vertical line shows bifurcation point at 61 K. **b**, Temperature dependence of the magnetic relaxation rate. Solid purple points are the relaxation rates extracted from AC susceptibility data (Table S5) and solid green points from DC magnetisation decay data (Table S8). Solid red line is given by $\tau^{-1} = \tau_0^{-1} \exp[-U_{\text{eff}}/kT] + CT^n$, dashed black line is given by $\tau^{-1} = \tau_0^{-1} \exp[-U_{\text{eff}}/kT]$ and dotted black line is given by $\tau^{-1} = CT^n$ with $U_{\text{eff}} = 1223 \text{ cm}^{-1}$ (1760 K), $\tau_0 = 1.986 \times 10^{-11} \text{ s}$, $C = 1.664 \times 10^{-6} \text{ s}^{-1} \text{ K}^{-n}$ and $n = 2.151$.

Figure 4 | *Ab initio* spin dynamics. **a**, Temperature dependence of the magnetic relaxation rate. Solid purple points are the relaxation rates extracted from AC susceptibility data (Table S5) and solid green points from DC magnetisation decay data (Table S8). Dashed black line gives the *ab initio* calculated Orbach relaxation rate and dotted black line gives the *ab initio* calculated Raman relaxation rate. **b**, Energy barrier to magnetic relaxation for **1**. Electronic states from CASSCF-SO calculations, labelled with their dominant m_J composition in the $J = 15/2$ basis (Table S20). Arrows represent the Orbach relaxation pathway at 150 K with $\sigma = 10 \text{ cm}^{-1}$, where the opacity of the arrows is proportional to the single-phonon transition probability normalised from each departing state and commencing with unit population in $|-15/2\rangle$; only relaxation pathways towards $|+15/2\rangle$ are shown (Table S24).



a**b**



a**b**